Influence of plate vibration on delamination formation in composites under multiple impacts

Huo, L.; Gong, X.; Cao, Z.; Zhang, M.; Cao, Y.; Li, X.; Tu, W.

DOI
10.1016/j.engstruct.2024.119336

Publication date
2025

Document Version
Final published version

Published in
Engineering Structures

Engineering Structures 324 (2025) 119336

Contents lists available at ScienceDirect

Engineering Structures

journal homepage: www.elsevier.com/locate/engstruct

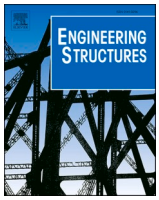

Influence of plate vibration on delamination formation in composites under multiple impacts

L. Huo [a], X. Gong [a], Z. Cao [a,b,*], M. Zhang [a], Y. Cao [c], X. Li [d], W. Tu [e,**]

[a] School of Mechanical Engineering, Northwestern Polytechnical University, Xi'an 710072, China
[b] NPU Xu Hang Electromagnetic Technology Limited Company, Xi'an 710100, China
[c] School of Aeronautics, Chongqing Jiaotong University, Chongqing 400074, China
[d] Department of Aerospace Science and Technology, Politecnico di Milano, Via La Masa 34, 20156 Milano, Italy
[e] Faculty of Aerospace Engineering, Delft University of Technology, P.O. Box 5058, 2600 GB Delft, The Netherlands

ARTICLE INFO

Keywords:
Polymer-matrix composites
Delamination
Impact behaviour
Quasi-static indentation
Finite element analysis

ABSTRACT

Dynamic vibration is believed to be a basic property of the impacted composite laminates; however, its effect on delamination formation requires further investigation. This study proposes a numerical model in collaborating with ABAQUS, which was calibrated using experimental results, to investigate the effect of plate vibration on delamination formation in composite laminates subjected to two consecutive identical ice or steel projectile impacts with a fixed loading distance. The only variable parameter for the different simulations was the time interval between the two impacts. The loading condition considered in this study is an extreme case where the composite laminate was still vibrating after the first impact when the second impact occurred. The results showed that the delaminations that formed later were significantly affected by the time intervals of the two identical successive ice or steel projectiles. As the vibrated impact points travel from the minimum peak to the adjacent maximum peak during the first vibration period, the newly formed delamination areas monotonically increase with time and vice versa. The change in the maximum contact forces of two identical impacts induced by dynamic vibration is suggested to be a major reason for the discrepancy between the newly formed delamination and previous ones.

1. Introduction

Fibre-Reinforced Polymer (FRP) composite laminates are widely used in many engineering applications [1–4], owing to their superior properties, such as high specific stiffness and strength [5–8]. However, FRP composite laminates are generally susceptible to out-of-plane concentrated loads (quasi-static indentation [9–11], low-velocity impact [12–14], high-velocity impact [15–17] and hyper-velocity impact [18,19]) owing to their weak interlaminar strength property [20]. Matrix cracking [21], fibre breakage [22] and delamination [23] are the three basic damage modes of FRP composite laminates under out-of-plane concentrated loads. In general, FRP composites belong to the brittle material category [24], and macroscopically, only the elastic and damage stages can be observed during the loading process of out-of-plane concentrated loads. The elastic behaviour of composite laminates under out-of-plane concentrated loading has a significant influence on the formation of damage; however, most studies have focused only on the damage stage of composites [25–28].

For a plate subjected to single out-of-plane concentrated loads, Olsson [29] suggested that three typical elastic plate responses can be distinguished macroscopically depending on the contact duration of the impactor and target plate. When the contact duration was of the same order as the transition time of through-the-thickness waves, three-dimensional wave propagation determined the plate response, and no obvious plate deformation was observed. The second type of plate response corresponds to a longer contact duration, and the plate response is influenced by the propagation of flexural and shear waves. When the contact duration was significantly longer than the time required for the induced waves to reach the boundaries of the plate, the plate response was similar to that of the quasi-static indented plate. The classification of out-of-plane concentrated loads proposed by Olsson was based on the global dynamic response of the target plate, which was

* Corresponding author at: School of Mechanical Engineering, Northwestern Polytechnical University, Xi'an 710072, China.
** Corresponding author.
E-mail addresses: czq66326@nwpu.edu.cn (Z. Cao), W.Tu@tudelft.nl (W. Tu).

https://doi.org/10.1016/j.engstruct.2024.119336
Received 29 July 2024; Received in revised form 25 October 2024; Accepted 16 November 2024
Available online 24 November 2024

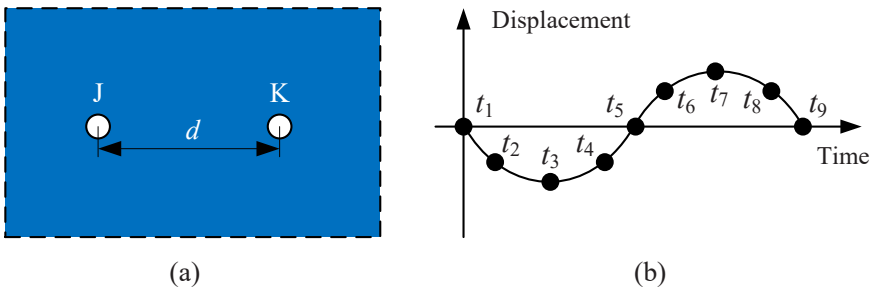

Fig. 1. (a) Illustration of a freely vibrating composite laminate with two points J and K on it, the distance between these two points is *d*; (b) any vibrational cycle of the points J or K due to impact in the out-of-plane direction.

determined by the contact duration. However, when considering the local dynamic response (local vibration) as the main factor in damage formation, in the authors' opinion, only two types of out-of-plane loads must be distinguished: quasi-static indentation and impact.

In the classification suggested by the authors, there is no local vibration for the target plate under quasi-static indentation, whereas local vibration is a basic characteristic of the impact case. This classification is necessary when multiple concentrated out-of-plane loads are considered. A typical example of multiple out-of-plane concentrated loads to which a composite structure can be subjected is multiple hail impacts associated with severe hailstorms. When hailstorms are considered to study multiple impacts, one must consider that hailstorms are characterised not only by many small hailstones over a certain duration of time, but also that these hailstones do not impact the same location, but rather are arbitrarily distributed in a certain area [30]. Therefore, the local dynamic vibration behaviour of an area on a composite laminate impacted by multiple hailstones can be affected by the impact of another hailstone in the adjacent area. In this extreme case, the damage formation within the former vibration area could be affected by the latter-impact induced local plate vibration.

Liu et al. [31] investigated the dynamic responses of corrugated cylindrical shells under nonlinear low-velocity impact using a newly proposed computational method. They successfully obtained the impact force of the shell structures using the proposed new method, which considered the Love thin shell theory and Hamilton principle. Subsequently, Liu et al. [32] proposed research on magneto-electro-thermo-mechanical loads on nonlinear forced vibrations in composite cylindrical shell structures, they developed a coupled nonlinear compactional method that considered the improved Donnell nonlinear shell theory and Maxwell static electricity/magnetism equations. With this method, the influence of parameters, such as external temperature change, magnetic potential, electric potential, etc., on the composite cylindrical shell nonlinear vibration response was successfully evaluated. Other related studies by Li et. al. [33] and Liu et. al. [34] also reported the investigations on the dynamic responses of different structures, and successfully predicted the impact forces using their developed computational methods, whereas they did not comprehensively investigate the effect of plate vibration on the formation of damage. In addition, a literature review by Sadighi and Alderliesten [35] showed that there is still a lack of relevant reports on such a topic that address how the damage formation is affected by the local dynamic vibration in a multiple impacted composite laminate.

As a first step toward overcoming this gap, this study developed a progressive damage finite element (FE) model in collaborating with ABAQUS to investigate the effect of local plate vibration on delamination formation in a composite laminate with multiple impacts. The multiple out-of-plane concentrated loads considered in this study were two successive identical ice or steel impacts applied at different locations with a fixed loading distance along the lengthwise centreline of the rectangular composite laminate. In this FE model, the Hashin matrix and fibre damage criteria [36] were adopted to simulate the initiation of matrix and fibre damage. The equivalent strain linear degradation fracture-mechanics-based damage evolution technology was used to consider the material stiffness degradation caused by the matrix and fibre damage. Delamination initiation and growth were modelled using the quadratic failure criterion [37] and the B-K delamination growth criterion [38], respectively. Ultrasonic C-scanning was performed to determine the projected delamination area which was subsequently used to calibrate the developed FE model.

Note that only the single steel projectile impact at the centre of the composite specimen was performed in the laboratory, and the measured projected delamination area was used to calibrate the established FE model. The single impact, rather than multiple impacts, was chosen to validate the FE model because the single impact has the advantage of being easy to control, and the impact location is more accurate. In addition, the choice of a steel projectile instead of an ice projectile is based on the consideration that the quality of the ice projectile generally varies greatly, even under ideal fabrication conditions. These different quality ice projectiles could induce different damage modes in CFRP laminates at the same impact velocity [39]. Therefore, to facilitate this investigation, a single-steel projectile impact test was conducted to validate the FE model in terms of damage formation.

2. Background

To further demonstrate the extreme multiple impact loading conditions investigated in this study, a composite laminate which can freely vibrate is shown in Fig. 1(a). This laminate has two arbitrary points, J and K, and the distance between these two points is *d*. When point J on the composite laminate was impacted, a cosine-curve-like local vibration was induced in the direction normal to the laminate surface (see Fig. 1(b)), whereas the flexural wave started to propagate outwards along the in-plane direction. As the flexural wave propagated to point K, a similar cosine curve-like local plate vibration occurred in the out-of-plane direction for the materials around point K (see Fig. 1(b)). The extreme multiple loading conditions considered in this study refer to the second impact applied at any time instant (any time instant between t_1 and t_9) during a vibration cycle at point K, as illustrated in Fig. 1(b). The out-of-plane vibration behaviour of point K is altered in this case; therefore, the damage formation in the area around this point could also be affected. It was assumed that the most dangerous case for point K corresponded to the second impact applied at time instant t_3. This loading condition can cause a larger displacement for the vibrated point on the plate than the corresponding single impact case, and this could lead to the most severe damage state. Note that the propagation of the in-plane wave is a natural response directly related to the membrane-bending coupling of the plate subjected to a concentrated out-of-plane impact load.

In general, hailstone has a layered structure and irregular shape [40], and spherical simulated hail ice (SHI) is typically adopted to investigate the hail impact damage resistance of composite laminates in a laboratory environment. Owing to the brittle nature of the SHI material and its

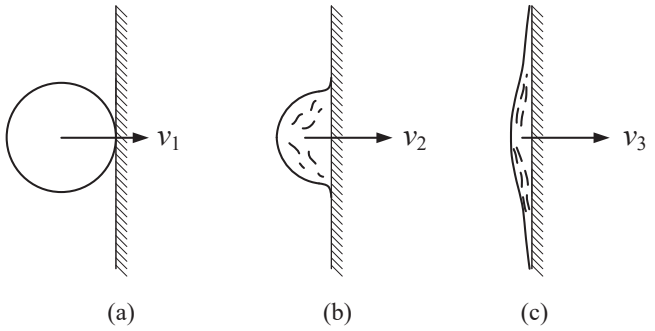

Fig. 2. Illustration of the characteristic failure behaviours of the SHI sphere during the impact: (a) phase I: initially contact; (b) phase II: partially shattered; and (c) phase III: totally shattered.

low tensile and compressive strengths, the SHI sphere can lose its integrity during impact. As illustrate in Fig. 2, when an SHI sphere impacts a fixed rigid wall and is completely shattered at the end of the impact process, three impact phases can be distinguished according to the integrity of the SHI sphere. In the impact phase I, the SHI sphere with an initial impact velocity began to contact the rigid plate, and compressive stress occurred in the contact area of the SHI sphere. This compressive stress dominates all stress components and can lead to compressive failure in the SHI sphere area. During the first impact phase, small cracks appear in the SHI sphere in the contact region. The next impact phase (impact phase II) is characterised by a partially shattered SHI sphere, and obvious cracks can be observed in the remaining solid part of the SHI sphere. The shattered part transformed into a fluid state. The last phase (phase III) corresponds to the fragmentation of the SHI sphere, which was completely transformed into small particles. To approximately model the impact behaviour of the SHI sphere, the characteristics of each impact phase should be considered.

Owing to the special impact behaviour of the SHI sphere, the peak impact force, which is a key parameter for delamination formation in a composite laminate, is approximately reached immediately after impact phase I (see Fig. 2(a)). Kim et al. [39] showed that the impact peak force for the SHI sphere generally increases with the impact velocity, and the greater the peak impact force, the more severe the delamination. This relationship between the peak force and damage formation was also reported by Zhou [41] for the steel impact. Therefore, this study hypothesises that the impact peak force varies with the impact moment of the second impact at point K (see Fig. 1(b)), such that the delamination area formed varies with the impact instant.

3. Numerical model

This section introduces the details of the constitutive models of ice and composite laminates. The constitutive model for ice is reproduced from the model reported by Tippmann et al. [40]. This ice model considered the strain-rate sensitivity and was validated with experimental results using strain-rate-dependent ice compression data. To model the impact behaviour of the composite laminate, a progress failure FE model which worked with a VUMAT user subroutine in ABAQUS was considered.

3.1. Constitutive model of ice material

The first to model ice material was Kim and Kedward [42], who adopted an elastic-plastic material model that considered a failure criterion based on hydrostatic tension. This model was then developed by considering the strain-rate dependent failure factors, which can accurately capture the features of the impact force corresponding to impact phase I as shown in Fig. 2(a). The ice model adopted in this study was reproduced from models developed in previous studies that considered a compressive strength that depends on the dynamic strain rate. This property was expressed as the strain-rate-dependent yield stresses of the ice model in ABAQUS. Specifically, the yield of the ice model occurred in the elastic phase, and element failure occurred when the hydrostatic tensile stress reached a threshold (tensile failure pressure) value independent of the strain rate. Subsequently, the failed elements behaved like a fluid because these elements can only withstand hydrostatic compression and tension. The properties of the ice material used in this study are summarised in Table 1, and the rate-dependent yield strength values are listed in Table 2. This ice model was applied using the built-in material constitutive model of ABAQUS; therefore, the data listed in Tables 1 and 2 were treated only as input values.

Table 1
Material properties of ice [40].

Young's modulus	$E = 9.38$ GPa
Poisson's ratio	$\nu = 0.33$
Density	$\rho = 0.9$ g/cm^3
Tensile failure pressure	P = 0.517 MPa
Yield stress	$\sigma = 5.2$ MPa

Table 2
Rate-dependent yield stress for ice [40].

Stress ratio	Strain rate (s^1)
1	0
1.01	0.1
1.495577759	0.5
1.709011483	1
2.204589242	5
2.418022966	10
2.913600725	50
3.127034449	100
3.622612208	500
3.836045932	1000
4.331623691	5000
4.545057415	10,000
5.040635174	50,000
5.254068897	100,000
5.749646657	500,000
5.96308038	1,000,000

3.2. Constitutive model of composite laminate

To model the impact response and damage behaviour of the composite laminate, the constitutive model should consider the damage occurring within the ply (matrix cracking and fibre breakage) and between plies (delamination). This section introduces the damage criteria adopted to simulate matrix cracking, fibre breakage, delamination initiation, and propagation. To model the progressive damage process of the ply, the equivalent strain linear degradation fracture mechanics-based damage evolution technology was adopted. This composite-layer constitutive model was coded in the ABAQUS VUMAT user subroutine to implement the functionality. The ABAQUS built-in Cohesive Zone Model (CZM) was used to model delamination at the composite interface.

3.2.1. Plies

The property of the ply material in this study was treated as transversely isotropic. Therefore, the corresponding degraded stiffness matrix C_d with five independent constants is given as follows:

$$C_d = \frac{1}{\Delta}\begin{bmatrix} \frac{1}{r_f E_{11}} & -\frac{\nu_{21}}{E_{22}} & -\frac{\nu_{31}}{E_{33}} & 0 & 0 & 0 \\ -\frac{\nu_{12}}{E_{11}} & \frac{1}{r_m E_{22}} & -\frac{\nu_{32}}{E_{33}} & 0 & 0 & 0 \\ -\frac{\nu_{13}}{E_{11}} & -\frac{\nu_{23}}{E_{22}} & \frac{1}{E_{33}} & 0 & 0 & 0 \\ 0 & 0 & 0 & \frac{1}{r_f r_m G_{12}} & 0 & 0 \\ 0 & 0 & 0 & 0 & \frac{1}{r_f r_m G_{23}} & 0 \\ 0 & 0 & 0 & 0 & 0 & \frac{1}{r_f r_m G_{31}} \end{bmatrix} \quad (1)$$

where r_f and r_m are the degradation factors to consider the ply stiffness degradation due to matrix cracking and fibre breakage, and the expressions for Δ, r_f and r_m are as follows:

$$\begin{cases} \Delta = 1 - r_f r_m \nu_{12}\nu_{21} - r_m \nu_{23}\nu_{32} - r_f \nu_{13}\nu_{31} - 2 r_f r_m \nu_{21}\nu_{32}\nu_{13} \\ r_f = (1 - r_{ft})(1 - r_{fc}) \\ r_m = \max\left\{(1 - 0.9 r_{mt})^2, (1 - 0.5 r_{mc})^2\right\} \end{cases} \quad (2)$$

where r_{ft}, r_{fc}, r_{mt}, and r_{mc} are the damage variables corresponding to fibre and matrix damage under tensile and compressive loading, respectively. These damage variables can be obtained using the equivalent strain damage evolution method expressed as follows:

$$r_n = \frac{\varepsilon^t_{eq,n}\left(\varepsilon_{eq,n} - \varepsilon^i_{eq,n}\right)}{\varepsilon_{eq,n}\left(\varepsilon^t_{eq,n} - \varepsilon^i_{eq,n}\right)}, n = \mathrm{ft}, \mathrm{fc}, \mathrm{mt}, \mathrm{mc} \quad (3)$$

where ε^i and ε^t (n = ft, fc, mt, mc) refer to the initial and final failure strain and their expressions are given below:

$$\begin{cases} \varepsilon^i_{eq,\,n} = \dfrac{X_s}{E_{0,k}} \\ \varepsilon^t_{eq,\,n} = \dfrac{2G_j}{X_s l_c} \end{cases} \quad (4)$$

where X_s is the strength of the fibre or matrix material and $E_{0,\,k}$ is the original modulus of the composite laminate along the considered direction. G_j (j = I, II, or III) is the critical fracture energy of mode I, II, or III. l_c is the element characteristic length used to eliminate mesh sensitivity [37]. The value of l_c was considered as the cube root of the volume of the element in this study.

Both the tensile and compressive failures of the fibres were modelled using the maximum stress criterion, which is expressed as follows:

$$\begin{cases} d_{ft} = \left(\dfrac{\sigma_{22}}{X_T}\right)^2, (\sigma_{22} > 0); \\ d_{fc} = \left(\dfrac{\sigma_{22}}{X_C}\right)^2, (\sigma_{22} < 0). \end{cases} \quad (5)$$

where d_{ft} and d_{fc} are the results corresponding to the fibre tensile and compressive damage, respectively, using the maximum stress criteria. X_T and X_C are the tensile and compressive strengths of the composite layer in the fibre direction, respectively. In addition, the Hashin criterion was used to model the matrix tensile and compressive failures, which are expressed as follows:

$$d_{mc} = \frac{1}{Y_C}\left[\left(\frac{Y_C}{2S_{23}}\right)^2 - 1\right](\sigma_{22} + \sigma_{33}) + \frac{1}{4S_{23}^2}(\sigma_{22} + \sigma_{33})^2 + \frac{1}{S_{23}^2}\left(\sigma_{12}^2 - \sigma_{22}\sigma_{33}\right) + \frac{1}{S_{12}^2}\left(\sigma_{12}^2 + \sigma_{13}^2\right), (\sigma_{22} + \sigma_{33} < 0) \quad (6)$$

Table 3
Material properties for IM7/8552 unidirectional laminate [43].

Ply properties	Density	$\rho = 1.6$ g/cm^3
	Young's modulus	$E_{11} = 161$ GPa, $E_{22} = E_{33} = 11.4$ GPa, $G_{12} = G_{13} = 5.17$ GPa, $G_{23} = 3.98$ GPa
	Poisson's ratio	$\nu_{12} = \nu_{13} = 0.32$, $\nu_{23} = 0.435$
	Ply strength	$X_T = 2326.2$ MPa, $X_C = 1200.1$ MPa, $Y_T = 111$ MPa, $Y_C = 199.8$ MPa, $G_s^C = 82.5$ MPa
Interface properties	Density	$\rho = 1.3$ g/cm^3
	Interface strength	$N = 60$ MPa, $S = 82.6$ MPa
	Critical fracture energy	$G_n^C = 0.2$ N/mm, $G_{IIc} = G_{IIIc} = 1.0$ N/mm

Note: *Values are estimated

$$d_{mt} = \frac{1}{Y_T^2}(\sigma_{22} + \sigma_{33})^2 + \frac{1}{S_{23}^2}\left(\sigma_{23}^2 - \sigma_{22}\sigma_{33}\right) + \frac{1}{S_{12}^2}\left(\sigma_{12}^2 + \sigma_{13}^2\right)^2, (\sigma_{22} + \sigma_{33} > 0) \quad (7)$$

where Y_T and Y_C are the tensile and compressive strengths normal to the fibre direction, respectively. S_{13} and S_{23} are the out-of-plane shear strengths of the composite layers.

3.2.2. Interfaces

The built-in CZM technique in ABAQUS was adopted in this study to model the delamination between two adjacent plies in the composite laminate. More specifically, delamination initiation was simulated using the stress-based quadratic failure criterion, whereas the growth of delamination was modelled using the energy-based Benzeggagh and Kenane (B-K) criterion.

The quadratic failure criterion with this expression given below:

$$\frac{\langle t_n \rangle^2}{N^2} + \frac{t_s^2}{S^2} + \frac{t_t^2}{S^2} = 1 \quad (8)$$

where N and S refer to the normal and shear strengths of the ply interface, respectively, t_n is the normal traction, t_s and t_t are the shear tractions. The compressive stress in the first item of Eq. (8) is not included in this criterion, as indicated by the Macaulay brackets.

The delamination propagation was modelled using the B-K criterion, which is expressed as follows:

$$G_n^C + \left(G_s^C - G_n^C\right)\left\{\frac{G_S}{G_T}\right\}^\eta = G^C \quad (9)$$

where G_S is the sum of the out-of-plane shear direction dissipated energies, and G_T is the total dissipated energy in all three directions, $G_s^C$and G_n^C are the critical shear and normal fracture energies, respectively. The coefficient η is recommended as 1.45 in this study [37].

4. Finite element analysis model

The finite element analysis was performed using a fully clamped IM7/8552 composite laminate with dimensions of 150.0 mm × 300.0 mm × 1.1 mm. The stacking sequence of this composite laminate is $[0/45/90/-45]_s$. The detailed material properties adopted by this FE model are summarised in Table 3.

To achieve the four-side clamped boundary conditions in the FE model, as shown in Fig. 3, all six degrees of freedom of the regions close to the plate edges were set to 0. These regions were marked as 'Fixed' in Fig. 3. Geometric nonlinearity was considered in the FE model to improve simulation accuracy. In addition, the composite layers were meshed with the C3D8I element, and the ply interface was modelled using the COH3D8 element. To improve the computational efficiency, the central area (impact area) of the model with dimensions of 60 mm × 210 mm was meshed with a higher density than the other regions. The element size in this region is 0.75 mm × 1.17 mm

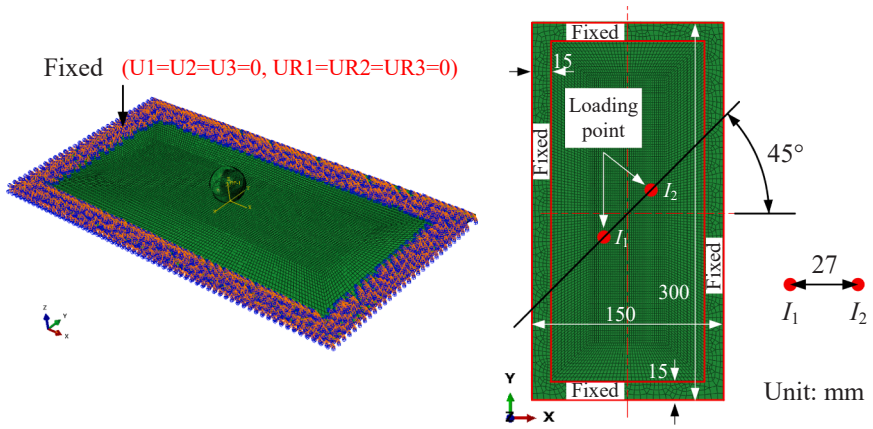

Fig. 3. Dimensions of the FE model that developed in this paper, the thickness of the composite laminate is 1.1 mm.

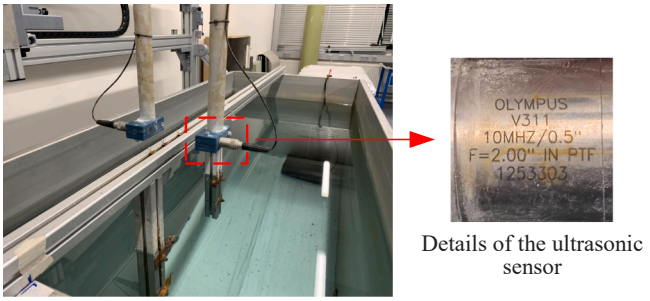

Fig. 4. Experimental setup for the ultrasonic C-scan and details of the ultrasonic sensor.

× 0.13 mm. The mensh sensitivity study showed that (the mesh sizes adopted were 1.5 × 2.34 × 0.13 mm, 0.75 mm × 1.17 mm × 0.13 mm, and 0.38 × 0.59 × 0.13 mm) with this mesh size of 0.75 mm × 1.17 mm × 0.13 mm the computational time was minimal and the simulation result (the projected delamination area) was close to the case which with higher mesh density. The thickness of the cohesive element in all regions was set to 0.003 mm. To reduce the zero-energy modes in the FE model, a relaxed-stiffness hourglass control method was considered.

The steel sphere projectile was treated as a discrete rigid body with a diameter of 25 mm and was meshed using the R3D4 element; the mass of the steel sphere was set to 0.064 kg. The contact between the steel sphere and composite laminate was a surface-to-surface type. The tangential contact behaviour was considered as a penalty type with a friction coefficient of 0.3 [44], and the normal contact was treated as the 'Hard' contact type. Furthermore, in this study, an SHI sphere with a diameter of 25 mm was considered and was meshed using C3D8R element. The global seed size used for meshing was 0.3. In addition, the normal contact behaviour settings in ABAQUS were identical to those in the steel-sphere impact FE model, whereas no friction was considered for the tangential contact behaviour. To consider the hourglass control of the SHI sphere impact, the linear and quadratic bulk viscosity parameters were set as 1.2 and 0 [40], respectively. Both the steel and SHI sphere impact FE models were solved using the ABAQUS/Explicit algorithm. The multiple ice impacts simulation was achieved using the Predefined Fields function, the initial state of the second impact can be set as any specific stage of the first impact outcomes using this function. In this study, the single SHI impact simulation was performed at the centre of the laminate (Fig. 3) to validate the FE model. After the FE model was validated, the steel and SHI impacts were applied at I_1 and I_2 on the numerical composite laminate, respectively, for the following investigations. Note that, as shown in Fig. 3, I_1 and I_2 are symmetric

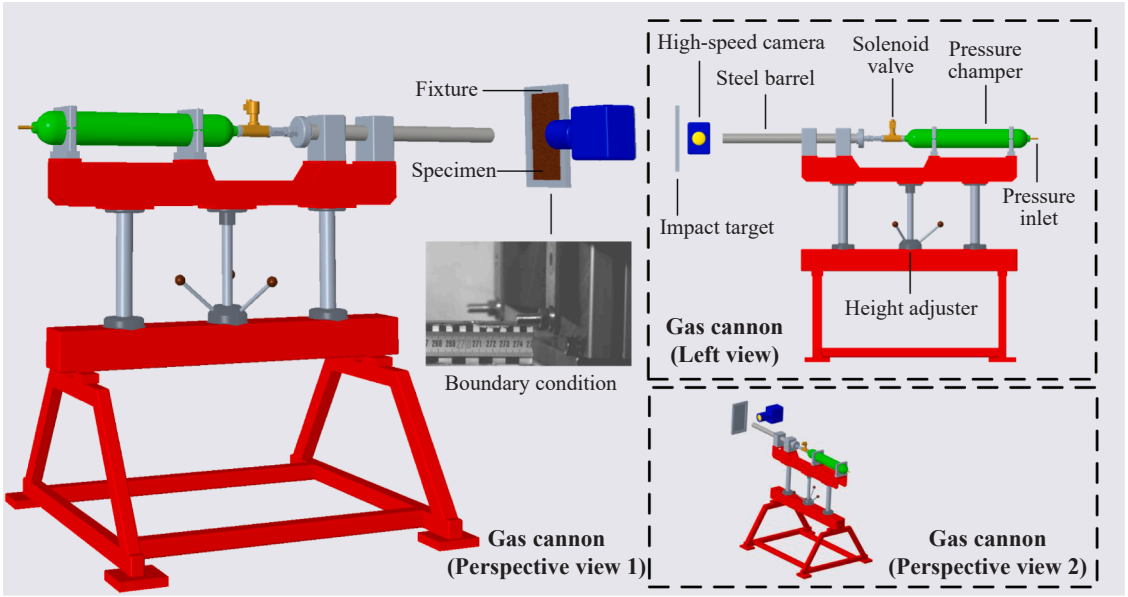

Fig. 5. Illustration of the gas gun test setup.

Fig. 6. Illustration of the steel head projectile.

about the centre of the composite laminate and on a line inclined 45°horizontally. The distance between these two impact locations was 27 mm.

5. Experimental details

Similar to the FE model, the composite specimens for the impact test had dimensions of 150.0 mm × 300.0 mm, a nominal thickness of 1.1 mm and a stacking sequence of $[0/45/90/-45]_s$. The specimens were cut from a 700.0 mm × 1400.0 mm composite panel that was made of the carbon/epoxy prepreg IM7/8552 supplied by the Hexcel Corporation. The composite panel was cured in an autoclave at a pressure of 7 bar and a maximum temperature of 180 ℃ for 120 min. Subsequently, all specimens were ultrasonically C-scanned before the impact tests, and specimens without defects were used for subsequent impact tests. The ultrasonic C-scan equipment used in this study is shown in Fig. 4 which has a large water tank and can be used to conduct damage detection for composite targets from the coupon level to the structural level. The designation of the ultrasonic sensor was designated as V311-SU and supplied by OLYMPUS with a detection frequency of 10 MHz. Details of the sensor are provided in Fig. 4.

In this study, a gas gun steel impact test was performed to calibrate the FE model in terms of the shape and size of the induced projected delamination area. To that and, a steel impact test platform based on a gas cannon was built, as shown in Fig. 5. The gas gun shown in Fig. 5 was designed to launching a 25 mm steel hemispherical impactor. To match the gas gun, as shown in Fig. 5, a projectile was designed. The base was polyethylene and fabricated using 3D printing technology, and the tip was made of 430F stainless steel. The total mass of the steel impactor was 0.064 kg which was the same as that of the FE model, and a maximum velocity of 150 m/s was reached with the gas gun. During the test, a solenoid valve was opened to release the pressurised gas, and then the steel projectile was accelerated via a 1 mm long steel barrel. After the projectile was moved out of the barrel and before it initially contacted with the specimen surface, a high-speed camera was used to record its trajectory, and the average velocity of the projectile was obtained indirectly (the distance between the end of the tube and the specimen surface was known). To match the four-side clamped boundary conditions similar to those of the FE model, as shown in Fig. 6, the composite specimen was fixed with bolts to a thin stainless-steel rectangular frame. A region with dimensions of 120.0 mm × 270.0 mm of the specimen was exposed to a steel projectile impact using this frame. The four-side clamped specimens were mounted vertically to ensure that the barrel axis was normal to the surface.

6. Validation of the FE model

In this study, the validity of the FE model was demonstrated in terms

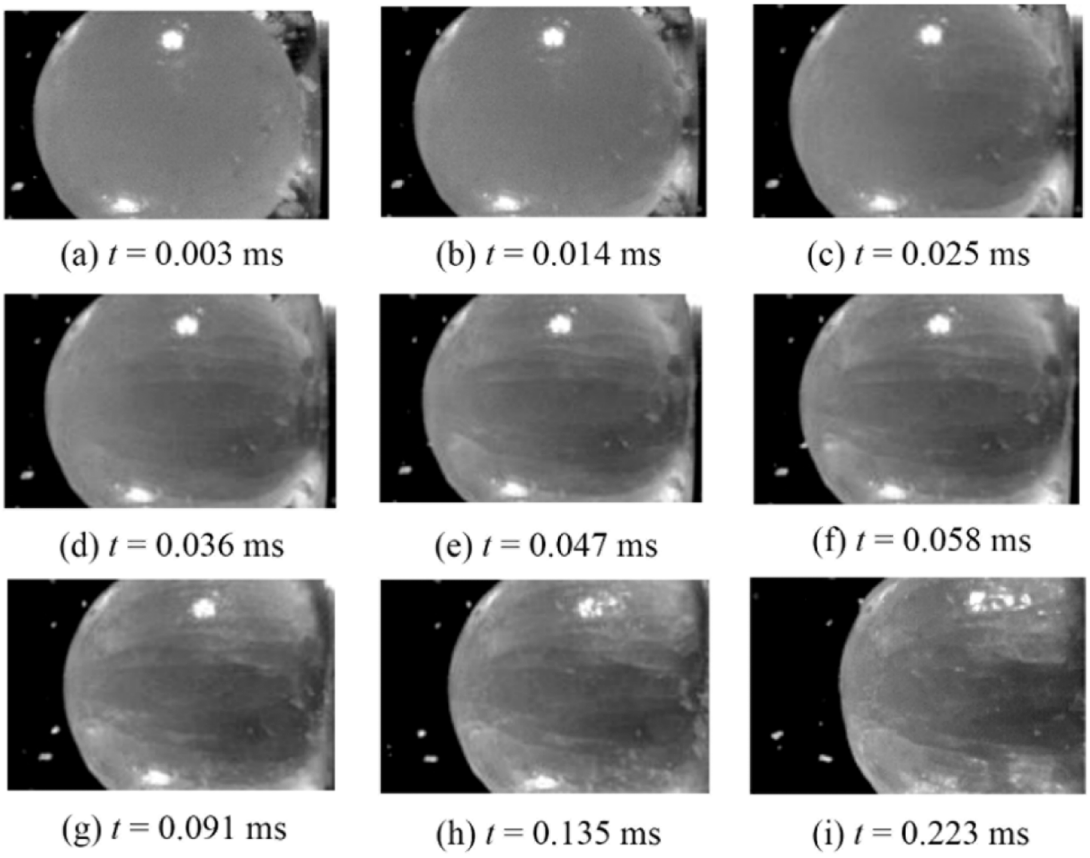

Fig. 7. Test result of the failure behaviour of the 50.8 mm diameter SHI sphere impact at a velocity of 60.6 m/s [40].

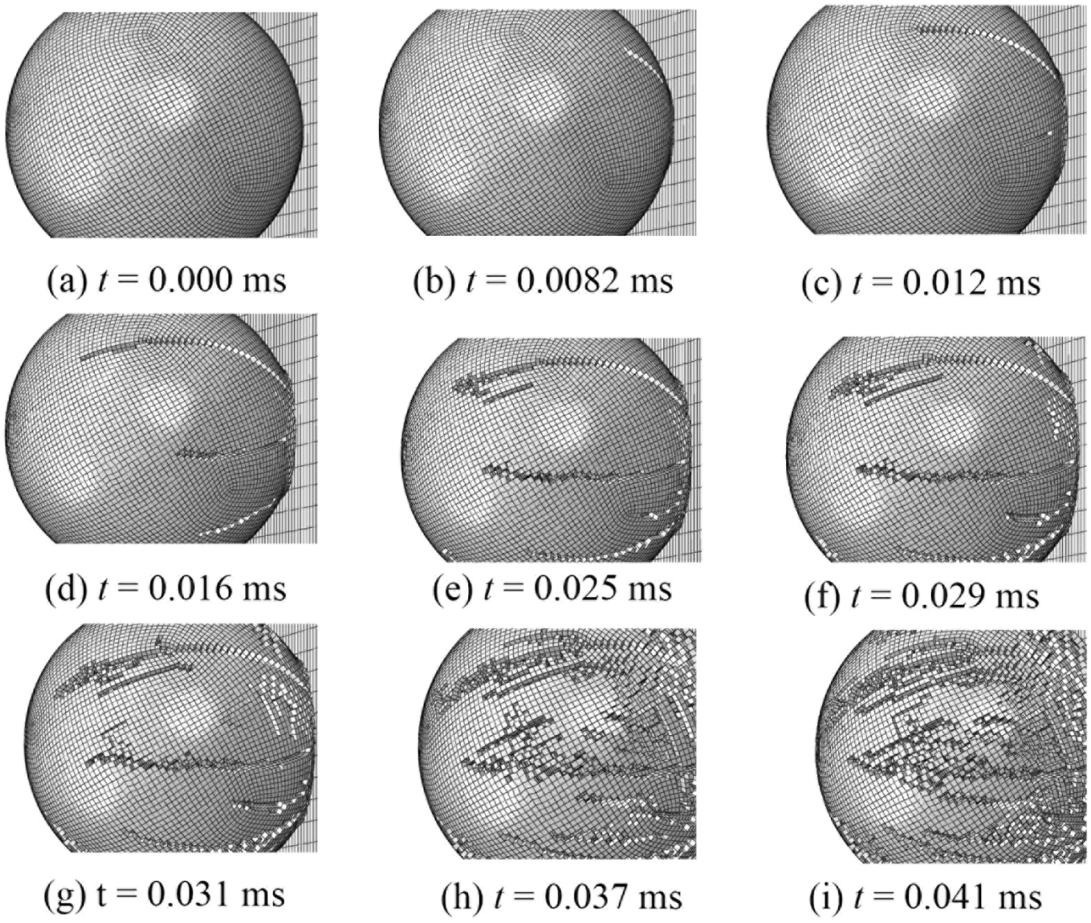

Fig. 8. Simulation result of the failure behaviour of the 25.0 mm diameter SHI sphere impact at a velocity of 60.6 m/s.

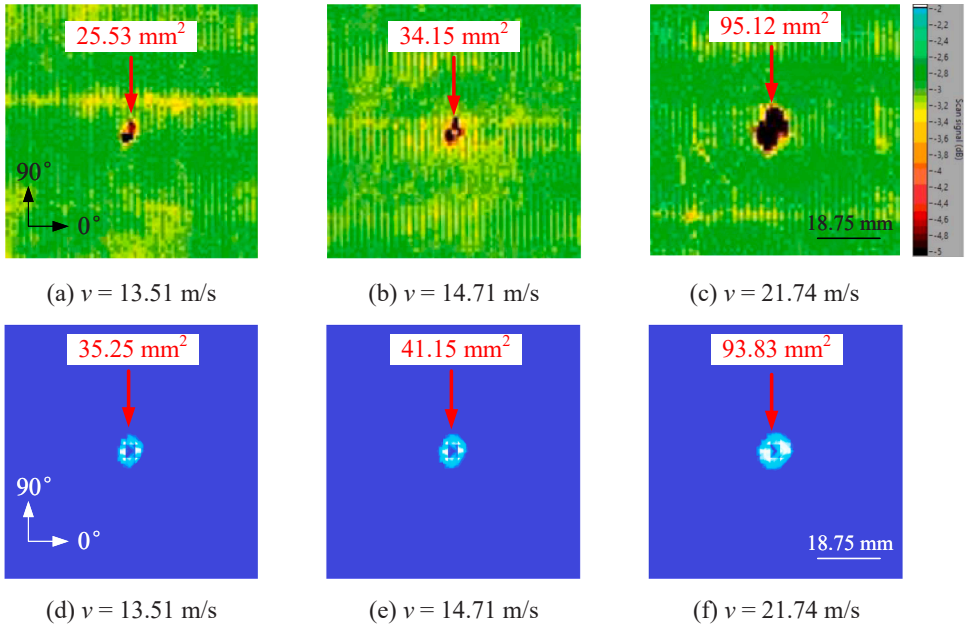

Fig. 9. Comparison of the experimental ((a)-(c)) and simulation ((d)-(f)) single impact projected delamination area of the CFRP laminates under various initial impact velocities (for typical damage sizes, the C-scan machine accuracy we adopted is on the order of 1–2 mm).

of the SHI sphere characteristic failure behaviour (see Fig. 2) and the delamination formation of the CFRP composite laminates under steel impact loading. In a study of [40], the failure features of crack initiation and crack propagation of a 50.8 mm diameter SHI sphere at a velocity of 60.6 m/s impact on the force measurement bar were clearly recorded. These high-speed camera records are shown in Fig. 7. For comparison,

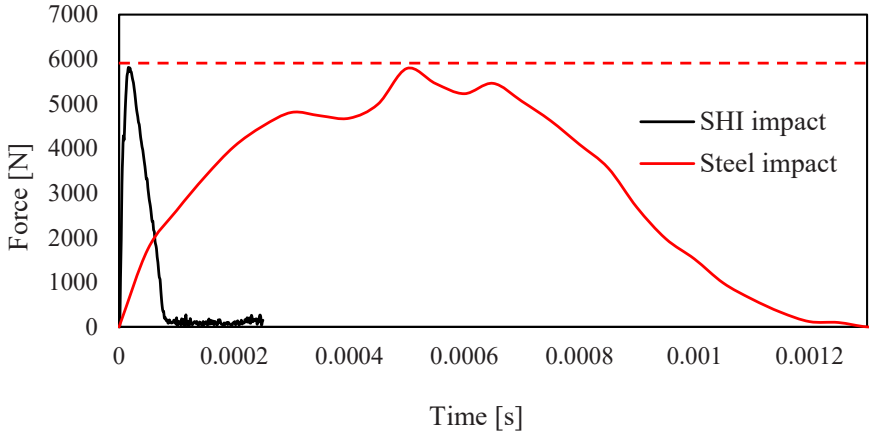

Fig. 10. Force–time curves of the steel and SHI impacts with similar peak impact forces, the impact velocities are 22 m/s and 99 m/s for the steel and SHI impacts, respectively.

the simulation results of a 25.0 mm diameter ice sphere impacting a rigid wall at a velocity of 60.6 m/s are provided in Fig. 8. A key conclusion can be drawn from Fig. 8 is that the developed FE model can capture the early stage physical phenomena of the failure features of the ice sphere during the impact. Therefore, the FE model can be used to qualitatively represent the ice-sphere failure progression of the impact. Because the adopted ice model has been quantitatively validated by comparing the simulation and experimental force–time curves in the study by Tippmann et al. [40], together with the good agreement between the failure features (Fig. 7 and Fig. 8), this study suggests that the ice model is physically sound and can be used to represent the real ice sphere impact.

To further demonstrate the validity of the FE model, the simulation and test results of the projected delamination areas of the composite laminates with different impact velocities were obtained and compared in Fig. 9. The actual impact locations in the FE model were determined by measuring the corresponding impact locations on the specimen surfaces. Besides, the initial velocity of the steel projectile should ideally be normal to the specimen surface; however, there is generally an avoided impact angle error (the impact velocity is not completely perpendicular to the specimen surface) owing to gravity. To facilitate the investigation, it was assumed that the impact velocities in the FE model were always normal to the surface of the composite laminate. This assumption is acceptable because of the short distance between the barrel end and front surface of the composite specimen, which was approximately 40 cm in this study. Fig. 9 shows that the projected delamination areas obtained using the FE model are similar to the corresponding test results, demonstrating the capability of the FE model in delamination area prediction. Note that the primary differences in the shape and area of the projected delamination regions are attributed to the error of the ultrasonic C-scan equipment (whose accuracy is on the order of 1–2 mm), measurement errors of the damage model parameters, and simplifications of the FE model.

7. Results and discussion

In this section, the numerical results of single-steel and SHI impacts with the same peak force were first compared to highlight the essential difference between these two impact events. Furthermore, multiple steel and ice impact results were analysed to demonstrate the influence of local dynamic vibrations on delamination formation. Accordingly, the multiple steel and ice impacts consisted of two successive single steel and SHI impacts with identical peak impact forces. Finally, the multiple steel and SHI impact results were compared to distinguish the differences in the local dynamic vibration effects on delamination formation.

Fig. 11. Projected delamination areas of the single steel impact with the velocity of 22 m/s at impact locations of I_1 and I_2, the delamination area of these two cases is 96.54 mm^2.

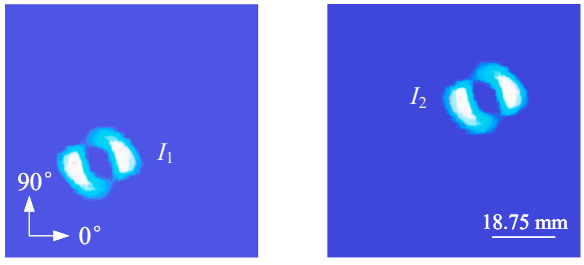

Fig. 12. Projected delamination areas of the single SHI impact with the velocity of 99 m/s at impact locations of I_1 and I_2, the delamination area of these two cases is 349.95 mm^2.

7.1. Single steel and SHI impact

Zhou [41] demonstrated that the peak impact force is a key parameter in delamination formation; therefore, similar peak impact forces associated with different impact events can induce similar delamination areas in the same composite laminate. To further investigate the influence of the peak force on delamination formation for different impact events, the simulation results of steel and SHI impacts with the peak force of 5800 N are compared in this section. To this end, the entire force–time curves of the steel and SHI impacts are shown in Fig. 10. The corresponding impact velocities for the steel and SHI impacts were 22 m/s and 99 m/s, respectively. Fig. 10 shows that although these two impact events have similar peak impact forces, the impact durations of these two impacts are significantly different, the SHI impact duration is 0.085 ms, and the steel impact duration is 1.25 ms. This discrepancy was primarily attributed to the different impact velocities of the steel and SHI impacts. Clearly, to obtain the same peak force level, the SHI impact

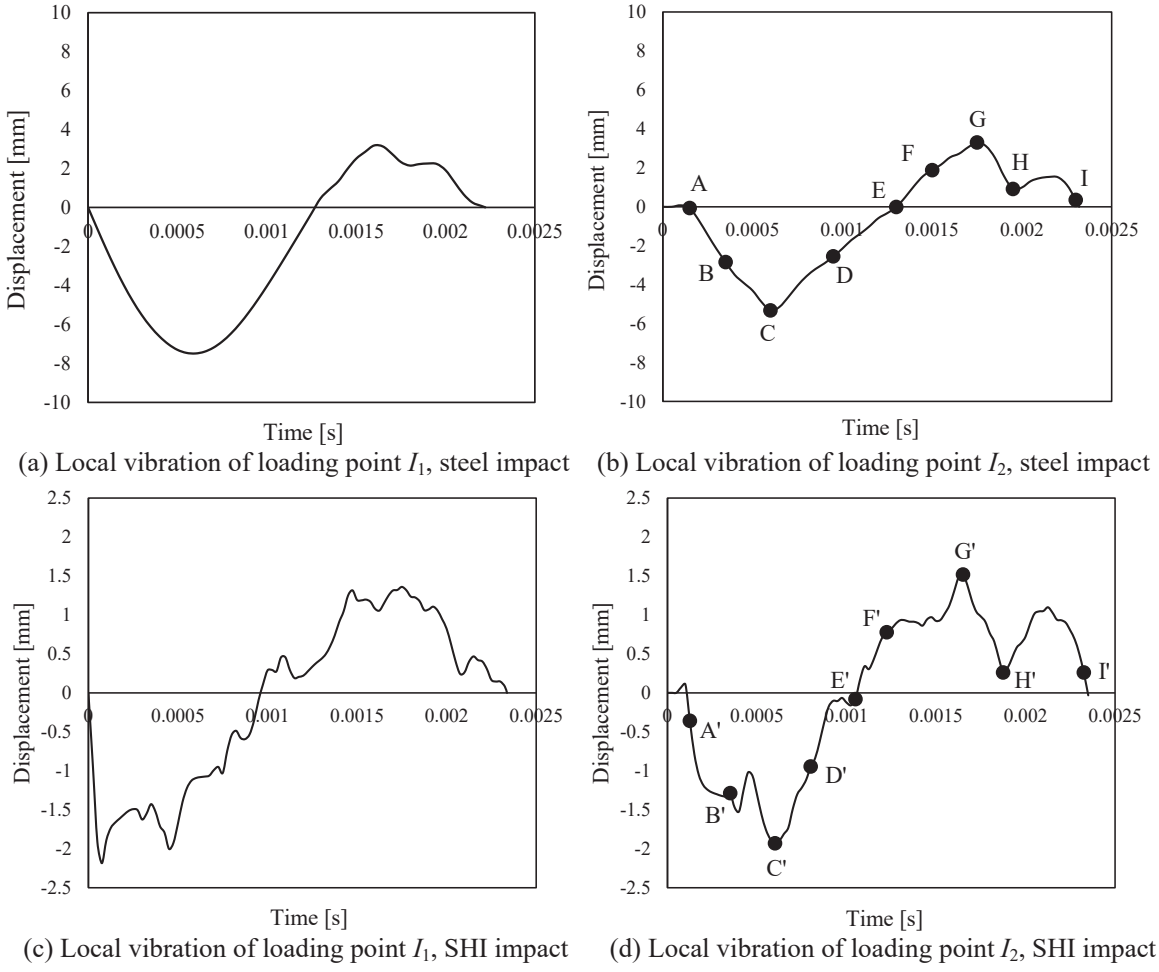

(a) Local vibration of loading point I_1, steel impact (b) Local vibration of loading point I_2, steel impact

(c) Local vibration of loading point I_1, SHI impact (d) Local vibration of loading point I_2, SHI impact

Fig. 13. Simulation results of the local vibrations of the loading point I_1 and I_2, the velocity of the multiple steel impact at I_1 and I_2 is 22 m/s, and for the multiple SHI impact at I_1 and I_2 is 99 m/s.

required a higher impact velocity.

To demonstrate the difference in the delamination formation of these two impact events directly, the corresponding projected delamination area of the two impact cases are presented in Fig. 11 and Fig. 12, respectively. Note that the impacts at locations I_1 and I_2 refer to two identical single steel or SHI impacts, whose force–time curves are accordingly shown in Fig. 10. Fig. 11 and Fig. 12 show that the projected delamination area shape of the steel impact is close to circular, whereas the SHI impact has an irregular elliptical shape and no delamination occurs within this central impact area. The SHI impact-projected delamination area had a size of 349.95 mm^2, which was approximately four times than that of the steel impact. In addition, the SHI impact velocity was 99 m/s, which was also approximately four times the steel impact velocity. This implies that the impact velocity is a more direct parameter than the peak impact force in delamination formation for different impact events. However, further studies are required to demonstrate this.

7.2. Multiple steel and SHI impact

When the loading point I_1 on the composite laminate was impacted (Fig. 3), a cosine-curve-like local vibration was induced along the out-of-plane direction. Subsequently, a similar local vibration occurs at loading point I_2. The corresponding simulation vibration curves of the steel and SHI impacts are presented in Fig. 13. Obviously, the reason for the I_2 vibration curves not being initiated from the origin coordinates is that time is required for the impact waves to propagate between I_1 and I_2. In addition, the steel impact vibration curves were smoother than the SHI impact curves, possibly due to the higher impact velocity of the SHI impact, which could induce more complex local vibration behaviours of the composite laminate. Note that the first vibration periods of loading points I_1 and I_2 were selected for the subsequent investigation. To well demonstrate the effect of local vibrations on the formation of delamination, nine moments were selected for the second steel or SHI impact according to the local vibration curves shown in Fig. 13(b) and (d). The specific time moments for the second steel or SHI impacts are

Table 4
Specific time moments for the second steel or SHI impact based on the local vibration curves of I_2.

Moment (t)	A	B	C	D	E	F	G	H	I
Value [10^{-4} s]	1.5	3.5	6.0	9.5	13.0	15.0	17.5	19.5	23.0
Moment (t)	A′	B′	C′	D′	E′	F′	G′	H′	I′
Value [10^{-4} s]	1.3	3.5	6.0	8.0	10.5	12.3	16.5	18.8	23.3

Note: the moment $t = 0$ s corresponds to the onset of the first impact

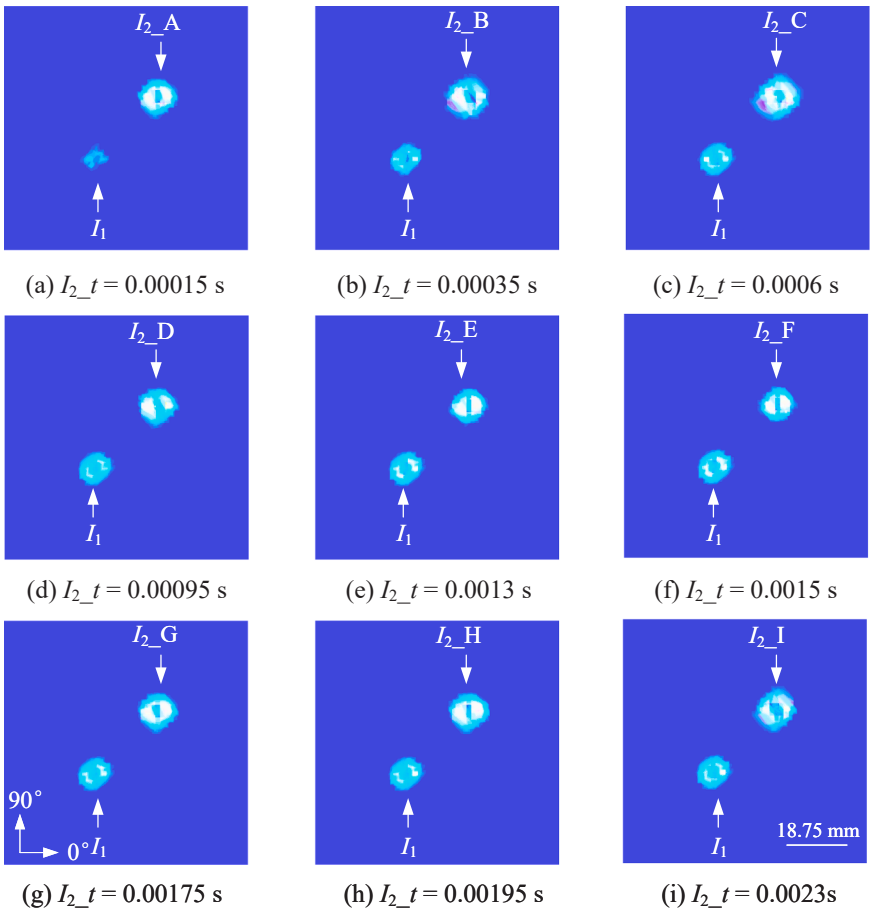

Fig. 14. Numerical projected delamination areas of the steel multiple impacts, the impact velocity is 22 m/s for the two impacts at I_1 and I_2.

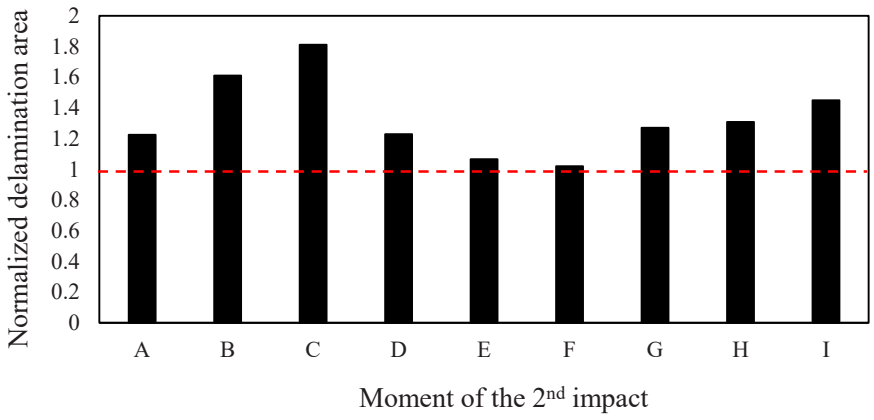

Fig. 15. Normalised delamination areas of the loading point I_2 under the steel impact, the impact velocity is 22 m/s for all second steel impact.

summarised in Table 4.

7.2.1. Numerical results of the multiple impact projected delamination area

The simulation results of the multiple steel impacts are shown in Fig. 14, and the projected delamination areas at the loading point I_2 with different impact moments were measured and shown in Fig. 15. Subjectively, compared with the first impact (the impact at loading point I_1), the projected delamination areas at loading point I_2 indeed vary with the second impact moment as shown in Fig. 14. The relationship between the measured delamination areas and the second impact moment shown in Fig. 15 can quantitatively demonstrates this statement. In Fig. 15, the normalised delamination area refers to the ratio of the projected delamination area of the second impact to that of the corresponding single steel impact projected delamination area. In addition, as shown in Fig. 16 and Fig. 17, the multiple SHI impact results show the same relationship between the second impact-projected delamination area and the second impact moment on multiple steel impacts.

As shown in Fig. 15, the second steel impact normalised delamination areas are larger than the first impact-projected delamination area. The steel impact normalised delamination area changes sinusoidally with the second impact moment which can be easily observed in Fig. 15. On the other hand, the sizes of the second SHI impact projected delamination areas were generally smaller than those of the first impact ones (Fig. 17) and varied randomly with the second impact moment. In

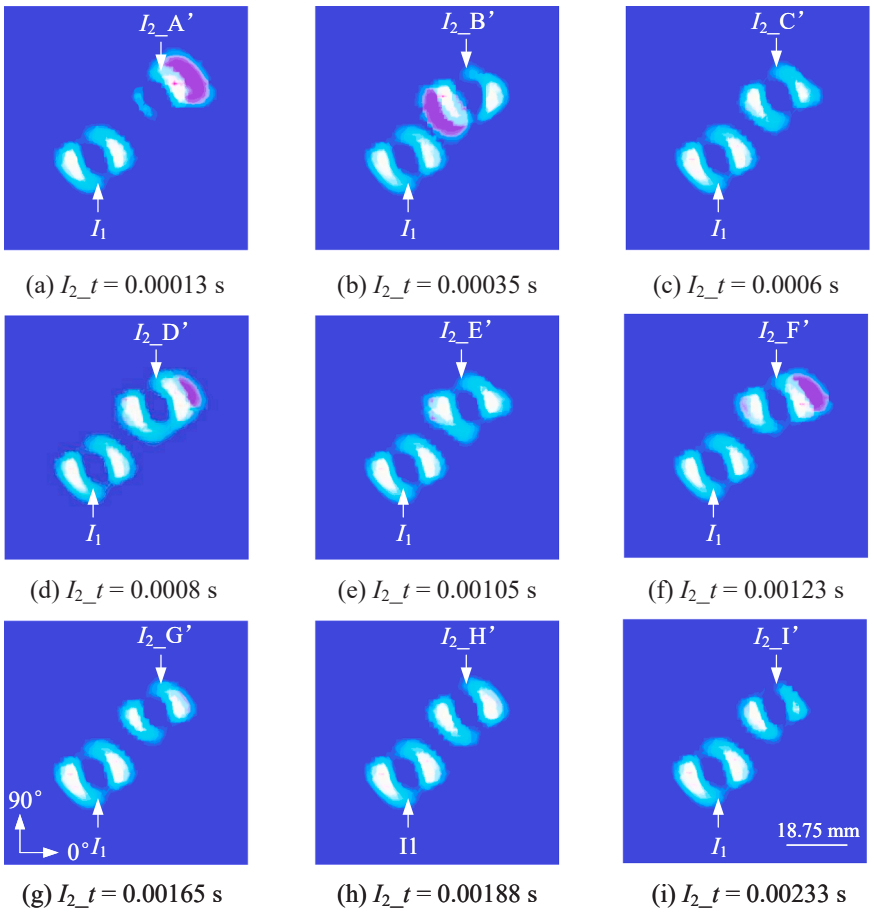

Fig. 16. Numerical projected delamination areas of the SHI multiple impacts, the impact velocity is 99 m/s for the two impacts at I_1 and I_2.

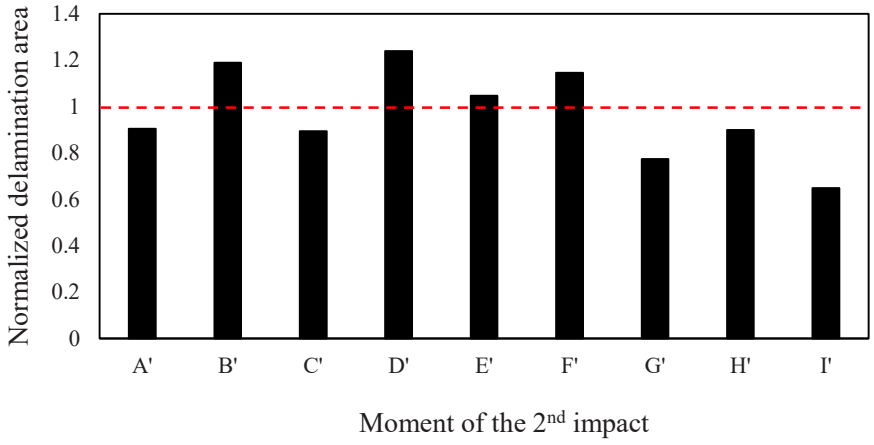

Fig. 17. Normalised delamination areas of the loading point I_2 under the SHI impact, the impact velocity is 99 m/s for all second SHI impact.

other words, although the second steel or SHI impact projected delamination area affected by the second impact moment, the influencing mechanisms were significantly different. Besides, it is worth noting that the projected delamination areas of loading point I_1 shown in Fig. 14(a) and (b) are significantly smaller than those in the single impact case. This is due to the technical limitations of the present ABAQUS software and the relatively long single steel impact duration (Fig. 10). At the second impact moment of $t = 1.5 \times 10^{-4}$ s (moment A), the first impact is still at this very beginning phase. However, ABAQUS has to terminate the calculation of the first impact at this moment and start the second impact simulation using the predefined field function. This finally resulted in the first impact simulations corresponding to those shown in Fig. 14(a) and (b) not being fully completed, and the projected delamination areas were relatively smaller than those in the single impact case. On the other hand, as shown in Fig. 16, the first SHI impact delamination area was the same for all multiple impact cases with different second impact moments. In this study, the single SHI impact duration was about 1.4×10^{-4} s (Fig. 10), whereas the earliest second impact moment (A′) of the multiple SHI impact was 1.3×10^{-4} s. In this case, the first SHI impact was almost complete when the composite laminate was subjected to the earliest second SHI impact. Therefore, the formation of the first SHI impact delamination is not affected by

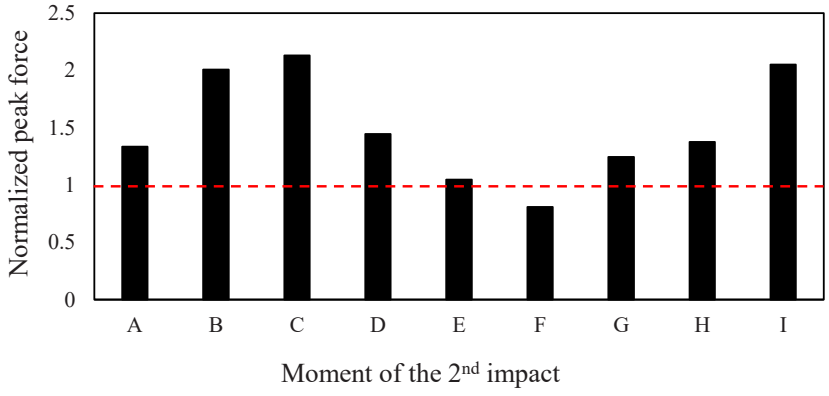

(a) Case of the multiple steel impact, the impact velocity is 22 m/s for all second steel impact

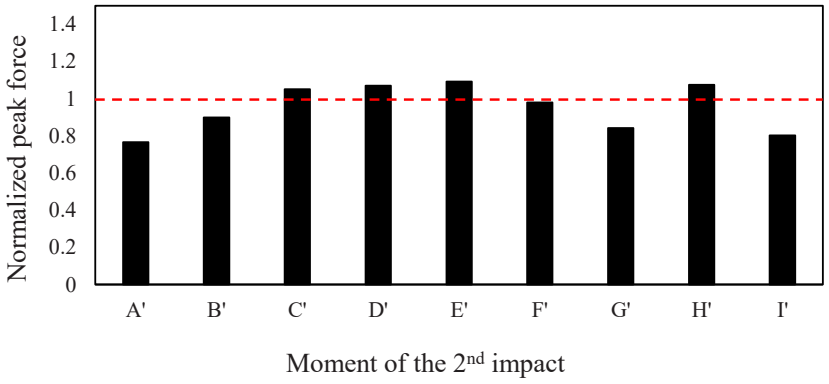

(b) Case of the multiple SHI impact, the impact velocity is 99 m/s for all second SHI impact

Fig. 18. Relationship between the normalised peak force and moment of the 2nd steel or SHI impact.

multiple SHI impacts.

7.2.2. Relationship between peak impact force and delamination formation

In the present study, the impact velocities for all second steel impacts and the SHI impact were set to 22 m/s and 99 m/s, respectively. This indicates that the impact velocity has no correlation with the discrepancy in the second impact projected delamination area of the steel impact or SHI impact cases, although the impact velocity has shown potential in terms of equivalent single steel and SHI impacts. Therefore, to determine the underlying reason why the same second steel or SHI impact induces different projected delamination areas at different impact moments relative to the first impact, the variation in the peak impact force with the impact moment and its relationship with the projected delamination area are discussed in this section. To this end, the peak forces of all the second impacts were obtained using the FE model and then normalised with the peak forces of the corresponding single steel or SHI impacts. The normalised impact peak forces of the second steel impact or SHI impact and their variation with the second impact moment are presented in Fig. 18. It can be concluded from Fig. 18 is that the normalised peak forces of multiple steel and SHI impacts vary sinusoidally with the second impact moment. For the multiple steel impact, similar to the second steel impacts normalised delamination area sizes (Fig. 15), almost all normalised peak forces shown in Fig. 18(a) are larger than the first impact projected delamination area, except for the impact moment F. Different from the multiple steel impact case, the sizes of the second SHI impact normalised peak force are slightly larger or smaller than the first impact normalised peak force (Fig. 18(b)).

To quantify the relationship between the normalised delamination area and the normalised peak force, a curve-fitting technique was adopted, and the final results are presented in Fig. 19. A linear relationship between the normalised delamination area and normalised peak force can be established for the second steel impact, which is in good agreement with the similar sinusoidal distributions of the normalised peak force and normalised projected delamination area shown in Fig. 15 and Fig. 18(a). On the other hand, the normalised delamination area and the normalised peak force of the second SHI impact showed a weak liner relationship, with $R^2 = 0.25$. The weaker linear relationship between the normalised projected delamination area and normalised peak force of the second SHI impact compared with that of the second steel impact could be attributed to the earlier failure of the SHI sphere during the impact or the more complex local dynamic vibration which is shown in Fig. 13(c) and (d).

In summary, the formation of the second steel or the SHI impact projected delamination area was affected by the second impact moment. This is because the second steel or SHI impact peak force is affected by the local dynamic vibration, with the assumption that peak impact force is a key parameter in delamination formation. Compared to the peak impact force, the impact velocity did not influence the formation of the second steel or SHI projected delamination; however, the impact velocity could be used to make equivalent between the steel and SHI impact events. In addition, the results of this study demonstrate that local dynamic vibrations have a significant influence on the formation of projected delamination in multiple impact cases. Designers should be aware that in extreme multiple impact cases, such as hail impacts, the same impact can cause more severe damage status due to the local dynamic vibration induced by the previous impact(s).

8. Conclusion

The influence of local dynamic vibration on the delamination formation of fully clamped composite laminates were investigated in this

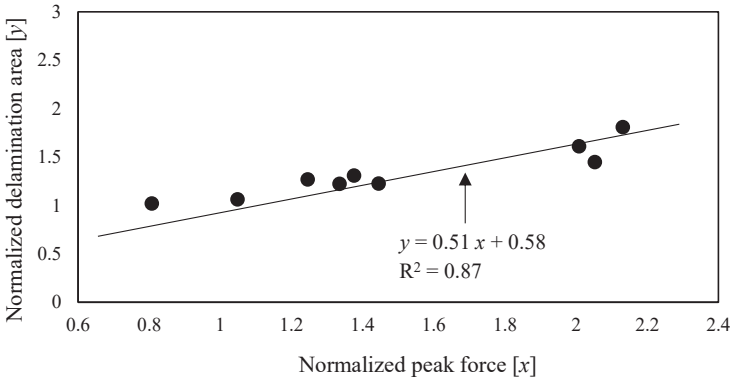

(a) Case of the multiple steel impact, the impact velocity is 22 m/s for all second steel impact

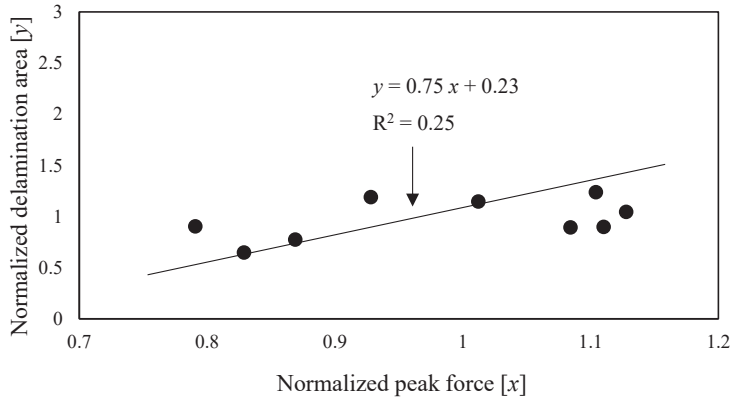

(b) Case of the multiple SHI impact, the impact velocity is 99 m/s for all second SHI impact

Fig. 19. Relationship between the normalised delamination area and normalised peak force.

study using a calibrated FE model. For the composite laminate subjected to two identical loads at different locations, the projected delamination formation associated with the second impact was significantly affected by the local dynamic vibrations induced by the first impact. The main conclusions are as follows:

- An experimental data validated progressive damage finite element (FE) model in collaborating with ABAQUS to investigate the influence of plate vibration on the formation of delamination for the multiple impacted composite laminate has been developed. This FE model is capable of modelling the failure process of the ice projectile and the damage behaviour of the composite laminates subjected to the out-of-plane ice and steel impacts.
- Both the second impact-induced projected delamination areas of the multiple ice and steel impact cases predicted by the FE model varied with the second impact moment relative to the first impact. The impact peak force in both cases also varied with the second impact moment. The change in the maximum contact forces of two identical impacts induced by dynamic vibration is suggested to be a major reason for the discrepancy between the newly formed delamination and previous ones.
- Similar peak impact forces cannot induce similar projected delamination areas in the single steel and SHI impact events. In contrast, the impact velocity showed this potential for equivalence in terms of the projected delamination area between the single steel and SHI sphere impacts in this study.

CRediT authorship contribution statement

Lubin Huo: Writing – original draft, Methodology, Investigation, Funding acquisition, Formal analysis, Data curation, Conceptualization, Resources, Funding acquisition, Project admission. **Xinglong Gong:** Writing – review & editing Investigation. **Zengqiang Cao:** Supervision, Resources, Project administration, Funding acquisition, Conceptualization. **Minghao Zhang:** Formal analysis. **Yuejie Cao:** Methodology. **Xi Li:** Formal analysis, Investigation. Wenjie Tu: Writing – review & editing, Methodology.

Declaration of Competing Interest

The authors declare that they have no known competing financial interests or personal relationships that could have appeared to influence the work reported in this paper.

Acknowledgement

The author would like to acknowledge the funding support for this research from the Fundamental Research for the Central Universities (D5000240092), the Key Research and Development Projects of Shaanxi Province (2022GXLH-02–25), the Xi'an Major Scientific and Technological Achievements Transformation Industrialization Project (23CGZHCYH0001), and the National Natural Science Foundation of China (52305146).

Data Availability

Data will be made available on request.

References

[1] Quan D, Deegan B, Alderliesten RC, Dransfeld C, Murphy N, Ivanković A, et al. The influence of interlayer/epoxy adhesion on the mode-I and mode-II fracture response of carbon fibre/epoxy composites interleaved with thermoplastic veils. Mater Des 2020;192:108781. https://doi.org/10.1016/j.matdes.2020.108781.

[2] Tao N, Anisimov AG, Groves RM. FEM-assisted shearography with spatially modulated heating for non-destructive testing of thick composites with deep defects. Compos Struct 2022;297:115980. https://doi.org/10.1016/j.compstruct.2022.115980.

[3] Zhang Y, Duan L, Liu H, Lu J, Huo Y. Experimental and numerical study on multi-impact performance of pre-damaged beams strengthened with CFRP. Eng Struct 2023;285:116034. https://doi.org/10.1016/j.engstruct.2023.116034.

[4] Luo Z, Wang H, Ng C-T, Fu J, Zhang Y, Wang C. On the low-velocity impact properties of CFRP/HAFRP interlayer hybrid fibre composite laminates. Eng Struct 2024;315:118387. https://doi.org/10.1016/j.engstruct.2024.118387.

[5] Azad MM, Kumar P, Kim HS. Delamination detection in CFRP laminates using deep transfer learning with limited experimental data. J Mater Res Technol 2024;29:3024–35. https://doi.org/10.1016/j.jmrt.2024.02.067.

[6] Li J, Sun Y, Yang S, Han Z, Shen G, Ma Z, et al. Revealing low temperature-mechanical coupling failure mechanisms in CFRP laminates with in-situ observations. J Mater Res Technol 2024;30:2817–25. https://doi.org/10.1016/j.jmrt.2024.04.022.

[7] Quan D, Urdániz JL, Ivanković A. Enhancing mode-I and mode-II fracture toughness of epoxy and carbon fibre reinforced epoxy composites using multi-walled carbon nanotubes. Mater Des 2018;143:81–92. https://doi.org/10.1016/j.matdes.2018.01.051.

[8] Quan D, Flynn S, Artuso M, Murphy N, Rouge C, Ivanković A. Interlaminar fracture toughness of CFRPs interleaved with stainless steel fibres. Compos Struct 2019:49–56. https://doi.org/10.1016/j.compstruct.2018.11.016.

[9] Wagih A, Maimí P, Blanco N, Costa J. A quasi-static indentation test to elucidate the sequence of damage events in low velocity impacts on composite laminates. Compos Part A 2016;82:180–9. https://doi.org/10.1016/j.compositesa.2015.11.041.

[10] Rao PM, Walter TR, Sankar B, Subhash G, Yen CF. Analysis of failure modes in three-dimensional woven composites subjected to quasi-static indentation. J Compos Mater 2013;48:2473–91. https://doi.org/10.1177/0021998313499950.

[11] Bulut M, Erkliğ A. The investigation of quasi-static indentation effect on laminated hybrid composite plates. Mech Mater 2018;117:225–34. https://doi.org/10.1016/j.mechmat.2017.11.005.

[12] Richardson MOW, Wisheart MJ. Review of low-velocity impact properties of composite materials. Compos Part A 1996;27:1123–31. https://doi.org/10.1016/1359-835X(96)00074-7.

[13] Feng Y, Wang Q, Yu Y, Zhang T, Wu D, Chen X, et al. Experimental-numerical-virtual (ENV) modelling technique for composite structure against low velocity impacts. Eng Struct 2023;278:115488. https://doi.org/10.1016/j.engstruct.2022.115488.

[14] Bogenfeld R, Kreikemeier J, Wille T. Review and benchmark study on the analysis of low-velocity impact on composite laminates. Eng Fail Anal 2018;86:72–99. https://doi.org/10.1016/j.engfailanal.2017.12.019.

[15] Yashiro S, Ogi K, Nakamura T, Yoshimura A. Characterization of high-velocity impact damage in CFRP laminates: Part I – Experiment. Compos Part A 2013;48:93–100. https://doi.org/10.1016/j.compositesa.2012.12.015.

[16] Heimbs S, Bergmann T, Schueler D, Toso-Pentecôte N. High velocity impact on preloaded composite plates. Compos Struct 2014;111:158–68. https://doi.org/10.1016/j.compstruct.2013.12.031.

[17] Hosur MV, Vaidya UK, Ulven C, Jeelani S. Performance of stitched/unstitched woven carbon/epoxy composites under high velocity impact loading. Compos Struct 2004;64:455–66. https://doi.org/10.1016/j.compstruct.2003.09.046.

[18] Pai A, Rodriguez-Millan M, Nishida M, Su Z, Shenoy BS. Numerical analysis of hyper velocity impact on quasi-isotropic carbon fiber reinforced polymer laminates. Acta Astronaut 2024;217:323–32. https://doi.org/10.1016/j.actaastro.2023.11.022.

[19] Appleby-Thomas GJ, Hazell PJ. The impact of structural composite materials. Part 2: hypervelocity impact and shock. J Strain Anal Eng 2012;47:406–18. https://doi.org/10.1177/0309324712448299.

[20] Körbelin J, Derra M. Influence of temperature and impact energy on low velocity impact damage severity in CFRP. Compos Part A 2018;115:76–87. https://doi.org/10.1016/j.compositesa.2018.09.010.

[21] Ouyang T, Sun W, Bao R, Tan R. Effects of matrix cracks on delamination of composite laminates subjected to low-velocity impact. Compos Struct 2021;262:113354. https://doi.org/10.1016/j.compstruct.2020.113354.

[22] Zhou J, Liao B, Zuo Y, Tuo H, Jia L. Low-velocity impact behavior and residual tensile strength of CFRP laminates. Compos Part B-Eng 2019;161:300–13. https://doi.org/10.1016/j.compositesb.2018.10.090.

[23] Johnson AF, Holzapfel M. Influence of delamination on impact damage in composite structures. Compos Sci Technol 2006;66:807–15. https://doi.org/10.1016/j.compscitech.2004.12.032.

[24] Huo L, Verstraeten D, Alderliesten RC. Assessment of two quasi-static approaches to mimic repeated impact response and damage behaviour of CFRP laminates. Chin J Aeronaut 2023;36:101–14. https://doi.org/10.1016/j.cja.2023.01.015.

[25] Jiang F, Guan Z, Li Z, Wang X. A method of predicting visual detectability of low-velocity impact damage in composite structures based on logistic regression model. Chin J Aeronaut 2021;34:296–308. https://doi.org/10.1016/j.cja.2020.10.006.

[26] Patil S, Mallikarjuna Reddy D. Impact damage assessment in carbon fiber reinforced composite using vibration-based new damage index and ultrasonic C-scanning method. Structures 2020;28:638–50. https://doi.org/10.1016/j.istruc.2020.09.011.

[27] Lu T, Chen X, Wang H, zhang L, Zhou Y. Comparison of low-velocity impact damage in thermoplastic and thermoset composites by non-destructive three-dimensional X-ray microscope. Polym Test 2020;91:106730. https://doi.org/10.1016/j.polymertesting.2020.106730.

[28] Shyr T-W, Pan Y-H. Impact resistance and damage characteristics of composite laminates. Compos Struct 2003:62. https://doi.org/10.1016/S0263-8223(03)00114-4.

[29] Olsson R. Mass criterion for wave controlled impact response of composite plates. Compos Part A 2000;31:879–87. https://doi.org/10.1016/S1359-835X(00)00020-8.

[30] Liu K, Li P, Wang Z. Statistical modeling of random hail impact. Extrem Mech Lett 2021;48:101374. https://doi.org/10.1016/j.eml.2021.101374.

[31] Liu Y, Hu W, Zhu R, Safaei B, Qin Z, Chu F. Dynamic responses of corrugated cylindrical shells subjected to nonlinear low-velocity impact. Aerosp Sci Technol 2022;121:107321. https://doi.org/10.1016/j.ast.2021.107321.

[32] Liu Y, Qin Z, Chu F. Investigation of magneto-electro-thermo-mechanical loads on nonlinear forced vibrations of composite cylindrical shells. Commun Nonlinear Sci Numer Simul 2022;107:106146. https://doi.org/10.1016/j.cnsns.2021.106146.

[33] Li H, Wang D, Xiao Z, Qin Z, Xiong J, Han Q, et al. Investigation of vibro-impact resistance of fiber reinforced composite plates with polyurea coating with elastic constraints. Aerosp Sci Technol 2022;121:107196. https://doi.org/10.1016/j.ast.2021.107196.

[34] Liu Y, Qin Z, Chu F. A nonlinear repeated impact model of auxetic honeycomb structures considering geometric nonlinearity and tensile/compressive deformation. J Appl Mech 2023:90. https://doi.org/10.1115/1.4062592.

[35] Sadighi M. Impact fatigue, multiple and repeated low-velocity impacts on FRP composites: A review. Compos Struct 2022;297:115962. https://doi.org/10.1016/j.compstruct.2022.115962.

[36] Hashin Z, Rotem A. A fatigue failure criterion for fiber reinforced materials. J Compos Mater 1973;7:448–64. https://doi.org/10.1177/002199837300700404.

[37] Li X, Ma D, Liu H, Tan W, Gao X, Zhang C, et al. Assessment of failure criteria and damage evolution methods for composite laminates under low-velocity impact. Compos Struct 2019;207:727–39. https://doi.org/10.1016/j.compstruct.2018.09.093.

[38] Benzeggagh ML, Kenane M. Measurement of mixed-mode delamination fracture toughness of unidirectional glass/epoxy composites with mixed-mode bending apparatus. Compos Sci Technol 1996;56:439–49. https://doi.org/10.1016/0266-3538(96)00005-X.

[39] Kim H, Welch DA, Kedward KT. Experimental investigation of high velocity ice impacts on woven carbon/epoxy composite panels. Compos Part A-Appl S 2003;34:24–41. https://doi.org/10.1016/S1359-835X(02)00258-0.

[40] Tippmann JD, Kim H, Rhymer JD. Experimentally validated strain rate dependent material model for spherical ice impact simulation. Int J Impact Eng 2013;57:43–54. https://doi.org/10.1016/j.ijimpeng.2013.01.013.

[41] Zhou G. The use of experimentally-determined impact force as a damage measure in impact damage resistance and tolerance of composite structures. Compos Struct 1998;42:375–82. https://doi.org/10.1016/S0263-8223(98)00089-0.

[42] Kim H, Kedward KT. Modeling hail ice impacts and predicting impact damage initiation in composite structures. AIAA J 2000:38. https://doi.org/10.2514/2.1099.

[43] Gan KW, Hallett SR, Wisnom MR. Measurement and modelling of interlaminar shear strength enhancement under moderate through-thickness compression. Compos Part A Appl Sci Manuf 2013;49:18–25. https://doi.org/10.1016/j.compositesa.2013.02.004.

[44] Huo L, Alderliesten RC, Sadighi M. Delamination initiation in fully clamped rectangular CFRP laminates subjected to out-of-plane quasi-static indentation loading. Compos Struct 2023;303:116316. https://doi.org/10.1016/j.compstruct.2022.116316.